Journal Pre-proof

Fabrication of an osmotic 3D printed solid dosage form for controlled release of active pharmaceutical ingredients

Christos I. Gioumouxouzis , Emmanouil Tzimtzimis ,
Orestis L. Katsamenis , Anthi Dourou , Catherine Markopoulou ,
Nikolaos Bouropoulos , Dimitrios Tzetzis , Dimitrios G. Fatouros

PII: S0928-0987(19)30449-X
DOI: https://doi.org/10.1016/j.ejps.2019.105176
Reference: PHASCI 105176

To appear in: *European Journal of Pharmaceutical Sciences*

Received date: 17 August 2019
Revised date: 14 October 2019
Accepted date: 3 December 2019

Please cite this article as: Christos I. Gioumouxouzis , Emmanouil Tzimtzimis , Orestis L. Katsamenis , Anthi Dourou , Catherine Markopoulou , Nikolaos Bouropoulos , Dimitrios Tzetzis , Dimitrios G. Fatouros , Fabrication of an osmotic 3D printed solid dosage form for controlled release of active pharmaceutical ingredients, *European Journal of Pharmaceutical Sciences* (2019), doi: https://doi.org/10.1016/j.ejps.2019.105176

This is a PDF file of an article that has undergone enhancements after acceptance, such as the addition of a cover page and metadata, and formatting for readability, but it is not yet the definitive version of record. This version will undergo additional copyediting, typesetting and review before it is published in its final form, but we are providing this version to give early visibility of the article. Please note that, during the production process, errors may be discovered which could affect the content, and all legal disclaimers that apply to the journal pertain.

© 2019 Published by Elsevier B.V.

Fabrication of an osmotic 3D printed solid dosage form for controlled release of active pharmaceutical ingredients

Christos I. Gioumouxouzis[1], Emmanouil Tzimtzimis[2], Orestis L. Katsamenis[3], Anthi Dourou[1], Catherine Markopoulou[1], Nikolaos Bouropoulos[4,5], Dimitrios Tzetzis[2], Dimitrios G. Fatouros[1,*]

[1]Laboratory of Pharmaceutical Technology, Department of Pharmaceutical Sciences, Aristotle University of Thessaloniki, GR-54124, Thessaloniki, Greece

[2]School of Science and Technology, International Hellenic University, 14km Thessaloniki - N. Moudania, Thermi GR57001, Greece

[3]μ-VIS X-ray Imaging Centre, Faculty of Engineering and Physical Sciences, University of Southampton, Southampton, United Kingdom.

[4]Department of Materials Science, University of Patras, 26504 Rio, Patras, Greece

[5]Foundation for Research and Technology Hellas, Institute of Chemical Engineering and High Temperature Chemical Processes, Patras, Greece

[*]Corresponding author: Dr Dimitrios G. Fatouros

e-mail: dfatouro@pharm.auth.gr

Tel: +302310997653

Fax: +302310997652

Journal Pre-proof

Journal Pre-proof

ABSTRACT

In pharmaceutical formulations, pharmacokinetic behavior of the Active Pharmaceutical Ingredients (API's) is significantly affected by their dissolution profiles. In this project, we attempted to create personalized dosage forms with osmotic properties that exhibit different API release patterns via Fused Deposition Modelling (FDM) 3D printing. Specifically, cellulose acetate was employed to create an external shell of an osmotically active core containing Diltiazem (DIL) as model drug. By removing parts of the shell (upper surface, linear lateral segments) were created dosage forms that modify their shape at specific time frames under the effect of the gradually induced osmotic pressure. Hot-Melt Extrusion (HME) was employed to fabricate two different 3DP feeding filaments, for the creation of either the shell or the osmotic core (dual-extrusion printing). Printed formulations and filaments were characterized by means of (TGA, XRD, DSC) and inspected using microscopy (optical and electron). The mechanical properties of the filaments were assessed by means of micro- and macro mechanical testing, whereas micro-Computed Tomography (μCT) was employed to investigate the volumetric changes occurring during the hydration process. XRD indicated the amorphization of DIL inside HME filaments and printed dosage forms, whereas the incorporated NaCl (osmogen) retained its crystallinity. Mechanical properties' testing confirmed the printability of produced filaments. Dissolution tests revealed that all formulations exhibited sustained release differing at the initiation time of the API dissolution (0, 120 and 360 min for the three different formulations). Finally, μCT uncovered the key structural changes assonated with distinct phases of the release profile. The above results demonstrate the successful utilization of an FDM 3D printer in order to create osmotic 3D printed formulations exhibiting sustained and/or delayed release, that can be easily personalized containing API doses corresponding to each patient's specific needs.

Journal Pre-proof

Keywords: additive manufacturing, 3D printing, osmotic system, controlled release, cellulose acetate, personalized medicine, micro- Computed tomography

Journal Pre-proof

ABBREVIATIONS

3DP	Three-Dimensional Printing
AM	Additive Manufacturing
API	Active Pharmaceutical Ingredient
CA	Cellulose Acetate
CAD	Computer Aided Design
DIL	Diltiazem
DSC	Differential Scanning Calorimetry
FDM	Fused Deposition Modeling
HME	Hot-Melt Extrusion
μCT	Micro-Computed Tomography
PVA	Polyvinyl Alcohol
PVP	Polyvinylpyrrolidone
SEM	Scanning Electron Microscopy
TEC	Triethyl Citrate
Tg	Glass Transition Temperature
TGA	Thermogravimetric Analysis
XRD	X-ray Diffractometry

Journal Pre-proof

Journal Pre-proof

1. INTRODUCTION

3D printing (3DP) or Additive Manufacturing (AM) is a novel technique of creating objects with easily customizable dimensions that has the potential to revolutionize manufacturing processes. Amongst the variety of the available 3DP methods, Fused Deposition Modelling (FDM) has been the most widely utilized in pharmaceutical research, in an attempt to create personalized dosage forms with elaborate shapes and modifiable dimensions (Gioumouxouzis et al., 2018a). FDM working principle is the layer-by-layer deposition of molten polymeric strands on a building plate, via a heated nozzle that moves at XYZ axis. Feeding of the heated nozzle is carried out using a polymeric filament that incorporates the active pharmaceutical ingredients (API's). Manufacturing of the API-loaded filament is usually facilitated by a Hot-Melt Extruder (HME), a device that mixes API's and excipients in a heated barrel via a rotating screw (Pietrzak et al., 2015).

Numerous research papers have been published during the last few years utilizing 3D printing to produce oral drug-loaded formulations presenting: i) a variety of release profiles, ii) incorporation of more than one API's or iii) usage of 3D prints as carriers for other pharmaceutical formulations (Gioumouxouzis et al., 2018a; Lim et al., 2018). The most interesting attempts include formulations that resulted from the utilization of 3D printers with multiple nozzles. Multiple nozzles enable the creation of dosage forms with increased structural complexity (facilitating the desired controlled release behavior of the API) (Gioumouxouzis et al., 2017; Kadry et al., 2018; Li et al., 2017; Okwuosa et al., 2017; Tagami et al., 2018), dosage forms that allow the dissolution of distinct API's at different release rates (Gioumouxouzis et al., 2018b; Goyanes et al., 2015; Pereira et al., 2019) or a combination of the above (Khaled et al., 2015a, 2015b). An important factor is that these elaborate drug-loaded formulations can be

Journal Pre-proof

created rapidly as a part of a one or two-stage procedure, making 3D printing an economically viable solution for the formulation of dosage forms with increased levels of complexity. Typical examples of such formulations are floating systems (including cavities) (Chai et al., 2017), delayed/sustained release dosage forms (containing coatings) (Okwuosa et al., 2017), osmotic pumps (Scoutaris et al., 2018) or dosage forms with "exotic" external shape (i.e. torus (Gioumouxouzis et al., 2017) or candy-like (Scoutaris et al., 2018)).

In the present work we attempted to create osmotically controlled 3DP dosage forms that consist of an external water-permeable shell and an API-containing osmotic core. The shell consists of cellulose acetate (CA), a cellulose derivative widely used to create semipermeable coatings (Verma, 2002), that has not been previously investigated in 3DP pharmaceutical research. The core consists mainly of polyvinyl alcohol (PVA) and osmogens (mannitol, NaCl) (Abd-Elbary et al., 2011), whereas Diltiazem (DIL) was chosen as a model drug, mainly due to its thermostability (Sorrenti et al., 2010) and the fact that it is a commonly used drug, incorporated in various forms of controlled release formulations ("BNF," 2014). The aim of the study was to demonstrate that the dosage forms' shell ruptures at specific points (were linear cavities have been introduced creating "weak spots" at the shell) under the effect of the increasing internal osmotic pressure. The "oyster-like" opening of the shell exposes the dissolvable core to the dissolution medium signing the initiation of the API dissolution into the medium. By introducing different number of linear cavities (single/double-caved formulations) or eliminating the entire top side of the CA cover, we created dosage forms presenting pressure-controlled release and thus time-controlled release of the API.

The aforementioned formulations indicate the potential of creating *in situ* complex drug delivery systems with personalized API content adjusted to the needs of individual patients. Moreover,

Journal Pre-proof

creation of such formulations highlights the potential of industrial manufacturing of complex systems in a rapid and economically efficient way, as it 3DP eliminates the majority of stages (i.e. coating, drilling) necessary to create a dosage form with elaborate structure (Kadry et al., 2018).

2. MATERIALS AND METHODS

2.1. Materials

Diltiazem HCl (MW: 450.978, water solubility at 25^{o}C 565 g/L at 25°C (Stepanovs et al., 2016)), NaCl (MW: 58.44, water solubility at 25^{o}C: 357 g/L (O'Neil, 2013)) and Mannitol (MW: 182.17, water solubility at 37^{o}C: 193.5 g/L (Yalkowsky et al., 2010)) were purchased from Fagron Hellas, Greece. Partially hydrolyzed PVA (Mowiol® 4-88, MW ~31,000), cellulose acetate (MW ~30,000) and triethyl citrate (TEC) were purchased from Sigma Aldrich Co Ltd (Germany). Polyvinylpyrrolidone (PVP) K30 (Kollidon®) was purchased from BASF (Germany). All chemicals were of analytical grade. Distilled water was used in all experimental procedures.

2.2. Preparation of filaments

2.2.1. Preparation of diltiazem-loaded PVA-based filament

A mixture containing 55% PVA, 20% DIL, 13% mannitol, 7% NaCl and 5% PVP K30 (total mixture weight 80 gr) was prepared and fed into a single-screw extruder (Filabot Original®, Filabot Inc., VT, USA). PVA and NaCl were grinded prior to mixing using a domestic grinder and sieved through a 850 μm mesh, to ensure absence of large particles inside the mixture. The extruder was operated at 35 rpm and the mixture was extruded at 165^{o}C through a custom drilled

1.6 mm nozzle. A commercial cooling fan was employed to ensure rapid cooling and homogenous diameter of the produced filament. Filaments were stored in a vacuum desiccator to avoid their exposure to moisture.

PVA was chosen as a carrier for both its acceptable 3D printing performance and its relatively slow water dissolution (at 37^{o}C) (Gioumouxouzis et al., 2017), preventing incorporated highly soluble DIL HCl from rapidly dissolving in the dissolution medium (McClelland et al., 1991). Mannitol was used as both plasticizer and osmotic agent (Abd-Elbary et al., 2011; Gioumouxouzis et al., 2018b), whereas NaCl was added to enhance osmotic properties of the formulation (Abd-Elbary et al., 2011; Verma, 2002). PVP K30 was used as a wicking agent to facilitate hydration of the dosage form's core (Verma, 2002). All mixture ingredients were used at concentrations that have shown to induce desired behavior attributed to their properties.

2.2.2. Preparation of CA-based filament

CA was plasticized with 25% TEC, as its high T_g required significant amount of plasticizer to facilitate HME. This amount of plasticizer was chosen to achieve good balance between flexibility and toughness of the filament (Mohanty et al., 2003; Park et al., 2004). Extrusion of the mixture was conducted at 180^{o}C through a custom made 1.6 mm nozzle at 35 rpm. Cooling fan was also employed during HME and produced filaments were stored in a vacuum desiccator.

2.3. Determination of DIL loading of PVA-based filaments

20 mg DIL were dissolved in 200 ml volumetric flasks creating a 100 mg/L stock solution. That solution was utilized to create five solutions used to obtain a reference curve (R^2=0.999). Subsequently, filament pieces weighting approximately 300 mg were selected from different parts of the extruded coils (to ensure to ensure uniform distribution of DIL in the entire filament)

Journal Pre-proof

and dissolved in 100 ml of distilled water. 2 mL of these solutions were transferred to 100 mL volumetric flasks and after that dilution, solutions were filtered with Millipore® Millex–HV PVDF 0.45 μm filters (Merck, Germany). The filtrate was used to determine DIL concentration according to the above reference curve, by employing a UV-2501PC spectrophotometer (Shimadzu, Japan) operating at 237 nm. Absorption of raw excipients was measured in a UV array at 237 nm and was found to be negligible at concentrations contained in the dissolution medium in comparison to diltiazem absorption.

Journal Pre-proof

2.4. Mechanical Tests

2.4.1. Instrumented Indentation Testing (IIT)

PVA- and CA-based filaments were assessed through indentation tests in order to compare their modulus and hardness. In instrumented indentation tests the load is measured as a function of penetration depth. Such tests enable local variations of modulus and hardness to be measured precisely (Mansour et al., 2013; Mansour and Tzetzis, 2013; Tzetzis et al., 2013). In the current work the indentations were conducted using a dynamic ultra-micro-hardness tester (DUH-211; Shimadzu Co., Kyoto, Japan), fitted with a triangular pyramid indenter tip (Berkovich indenter), which created indentations on the surface of the filaments under study that appeared as an equilateral triangle. The indentation hardness was automatically converted to hardness Vickers by the software of the apparatus. After contact of the indenter with the surface, this was driven into the surface until a peak load of 150 mN was reached. The peak load was held for 3 s (in order to minimize the effect of viscoelastic deformation of the specimen, notably creep, on property measurements) and then the indenter was unloaded, to a load of zero. Ten measurements, purposely scattered on the surface, were conducted on each specimen.

2.4.2. Tensile Tests

Tensile tests were performed at room temperature (23°C) on a Testometric (UK) universal testing machine at a constant crosshead speed of 0.5 mm/min. The modulus was calculated within the linear part of the stress–strain curves. All presented data correspond to the average of at least four measurements.

2.5. 3D printing of osmotically controlled formulations

3D printed dosage forms were designed as CAD files using AutoCAD 2016® (Autodesk Inc., USA) and exported as .stl files to Makerware® software version 3.9.2 (MakerBot Inc., USA).

Three caplet-shaped formulations were designed. All three formulations consisted of i) an osmotic core printed using the DIL-loaded PVA-based filament and ii) an external shell (thickness 0.06 cm) printed with the CA-based filament. The first formulation was printed without the upper surface of the CA shell (open top - formulation A). The second one had a whole shell, with a narrow linear cavity (0.2 mm wide) introduced at a certain point of the shell (at the point where shell's upper part begins -formulation B). Finally, the last formulation was similar to the former one with an additional second linear cavity introduced at the lower part of the formulation (formulation C) (Figure 1). Moreover, in formulations B and C a circular opening (d=1.3 mm) was introduced to both top and bottom sides of the formulations' shells to accelerate water permeation inside the core.

Core dimensions were calculated as following: Length and height of the core were arbitrary set to be 1.5 cm and 0.5 cm respectively. Several cores were printed with widths ranging from 0.4 to

Journal Pre-proof

0.7 cm and consequently weighted, establishing the following linear equation, correlating core mass with core width of the formulation:

m_c=1025w_c-105.8 (R^2=0.982), (1) where m_c=core mass (mg) and w_c=core width (cm).

Filament drug content was measured to be 97.5% of the theoretically incorporated drug content, so m_c should be 461.54 mg in order the core to contain 90 mg of DIL (for DIL core concentration 20% w/w).

Therefore, taking Eq. (1) into consideration core width (w_c) of the formulations should be 0.553 cm.

Printing was performed in a MakerBot Replicator® 2X 3D printer (MakerBot Inc., NY, USA), using the first nozzle for printing CA-based external shell and the second nozzle for printing DIL-loaded, PVA-based core. The following settings were employed:

i) CA-based shell printing nozzle: T_{print} = 215°C; ii) PVA-based core printing nozzle: T_{print} = 205°C;

iii) General: *Printing speed* = 20 mm/s, *First layer printing speed* = 7 mm/s, *Travel speed* = 150 mm/s, $T_{platform}$ = 115°C, *Infill density* = 100%, *Layer height* = 0.2 mm, *Number of shells* = 2, *Floor thickness* = 0 mm, *Roof thickness* = 1.2 mm, *Raft option* = Deactivated.

Purging walls option was activated (required for dual extrusion 3D prints, although increasing material waste, as it ensures minimization of printing defects - Figure 2C).

Additionally, to overcome oozing issues, resulting from short-duration immobilization of the nozzles during printheads' interchange, two tiny columns were added to the .stl design. The function of these columns was to absorb the over-deposition of PVA-based material at the edges of the dosage form (that could compromise the integrity of the CA-based shell), as the

Journal Pre-proof

immobilization of the printheads was taking place on their surface and not at the corners of the printed dosage form (Figure 1 & 2C).

To facilitate 3D printing building plate was covered with Blue painter's tape (3M, MI, USA) to ensure proper adhesion of the CA-based lower layers to the printing surface.

The dimensions of the 3D printed formulations (Figure 1C & D) were measured using a Kreator digital caliper (Varo, Belgium) and their images were acquired using an Ixus 1000 HS (Canon, Japan) camera.

2.6. Scanning Electron Microscopy, Optical Microscopy and Elemental Analysis studies

The morphological features of the extruded filaments and 3D printed tablets were assessed through a Phenom ProX (ThermoFisher Scientific, MA, USA) instrument, equipped with an optical microscope with a magnification range of 20 - 135x and a scanning electron microscope (SEM) with a thermionic CeB6 source, as well as a fully integrated Energy Dispersive Spectrometer (EDS) detector. The specimens were attached on a metal stub with double sided carbon tape (Ted Pella, USA) and inserted in the scanning electron microscopy's vacuum chamber using a special charge reduction sample holder. The sample holder is designed to reduce sample charging and eliminate extra sample preparation of non-conductive samples. The dedicated software package ProSuite PC (ThermoFisher Scientific, MA, USA) was used for the instrument control.

2.7. Physicochemical characterizations

2.7.1. Thermogravimetric analysis (TGA)

Journal Pre-proof

Thermogravimetric analysis (TGA) was performed using a TGA-50 (Shimadzu, Japan) apparatus equipped with a TA-60WS thermal analysis workstation, at a heating rate of 10°C/ min from 40°C to 500°C in nitrogen environment, at a 40 mL/min purge gas flow rate, using aluminum pans. All samples were run in triplicates.

2.7.2. Differential scanning calorimetry (DSC)

The thermal behavior of the samples was analyzed on a 204 F1 Phoenix DSC apparatus (Netsch GmBH, Germany). Five mg of the samples were sealed in aluminum pans with perforated lids and their DSC profiles were acquired from 35°C to 350°C at a heating rate of 10°C/min under a nitrogen purge of 70 mL/min. The software used for DSC measurements was Proteus ver. 5.2.1 (Netsch GmBH, Germany). All samples were run in triplicates.

2.7.3. X-ray Powder diffraction (XRD)

Sample crystallinity was evaluated using a powder X-ray diffractometer (D8-Advance, Bruker, Germany) with Ni-filtered CuKα1 radiation (λ = 0.154059 nm), operated at 40 kV and 40 mA. Samples were scanned from 5° to 50° at a step of 0.02° and a scan speed of 0.35 sec/step.

2.8. *In vitro* release studies

In vitro dissolution studies were conducted in 900 mL vessels at 37 ºC, using USP II dissolution paddle apparatus (PT-DT7 Pharma Test AG, Germany) rotating at 75 rpm, according to USP40-NF35 specifications (Kadry et al., 2018). The dissolution medium was distilled water and each experiment was conducted in triplicate (n=3). Samples (2 mL) were withdrawn at 10, 20, 30, 60, 90, 120, 180, 240, 360, 480, 600, 720 and 1440 min and replaced with an equal volume of

Journal Pre-proof

dissolution medium to maintain the sink condition. More frequent sampling (adding sampling points) than recommended was conducted in order to fully depict the dissolution behavior of the novel formulations. Consequently, samples were filtered through 0.45 μm filters mentioned in Section 2.3 and UV absorption of the filtrates was measured in the aforementioned Shimadzu UV-2501PC spectrophotometer at 237 nm. The acquired dissolution curves were assessed with DDSolver software (Zhang et al., 2010), in order to determine which dissolution model (Higuchi, Zero-order, First-order, Korsmeyer-Peppas, Hixson-Crowell, Hopfenberg, Quadratic, Gompertz, Peppas-Sahlin), best fits each one of them. Moreover, similarity factor (f_2) was calculated using the same software, in an attempt to compare the similarity of the dissolution profiles of each formulation.

Journal Pre-proof

2.9. Time lapsed X-ray microfocus computed tomography (μCT) imaging

Time-lapsed X-ray microfocus computed tomography (μCT) was used to assess the internal structure and the dissolution behavior during hydration of the dosage form type with the highest degree of complexity (Form A). Hydration of the printed dosage form (form A) was conducted *ex situ* in 900 mL borosilicate beaker at 37 °C with gentle steering. The dissolution medium was distilled water and the printer form was imaged consequently at 0, 100, 200 and 400 min exposure to water. In order to minimize disruption of hydration process, a fast-acquisition protocol was developed, which enabled imaging in 12 min.

μCT imaging was performed using Nikon's Med-X prototype micro-CT scanner (Nikon Metrology UK Ltd) at the Biomedical Imaging Unit at University Hospital Southampton. Imaging was conducted at 80 kVp / 124 μA without any beam pre-filtration. The source to detector and source to object distances were 992.0 mm and 49.6 mm respectively, resulting in a voxel size of 20 μm. Imaging parameters were as follows: 1401 projections were taken over the 360 degrees rotation, with 2 frames per projection being averaged to improve the signal to noise ratio. Exposure time of each projection was 250 ms and the detector's gain was set to 30 dB. After CT acquisition, the data were reconstructed into 32-bit volume files by means of Nikon's own reconstruction software (CT Agent, v. XT 5.1.4.2 MedX 1; Nikon Metrology, Tring, UK), which uses a filtered-back projection algorithm. The reconstructed 32-bit raw image volumes were then converted to 8-bit volumes for visualization and quantification.

3D semi-automatic segmentation was carried out in ITK-Snap (v. 3.6.0 -alpha), an open source software medical image processing platform focusing on segmentation and analysis of 2D and 3D datasets using snake evolution algorithms (Yushkevich et al., 2006). ITK-Snap software was run on University of Southampton's IRIDIS 5 high performance visualisation cluster. Segmentation of the different image components (namely: the CA-shell and the dry and hydrated core) was achieved using classifiers which were previously trained to discriminate between the aforementioned image components. The training was done by manually selecting representative regions from each "class" of features, and the segmentation algorithm was run under supervision. Intervention and manual refinement of the segmentation took please when to prevent leakage of the segmentation to neighboring classes. Visualization of the segmentation was carried out in ITK-Snap, while volume rendering of the dosage form at the different hydration time intervals was done in Volume Graphics VGStudioMAX.

Journal Pre-proof

2.10. Statistical Analysis

Data were analyzed using Student's t test. Significance level was set at $p < 0.05$.

3. RESULTS AND DISCUSSION

3.1. HME procedure

HME of both PVA-based and CA-based mixtures was performed successfully. Filament pieces with acceptable diameter variation (1.75 ± 0.07 mm) were selected for 3D printing. Both filament types exhibited excellent mechanical properties macroscopically (with CA-based filament presenting behavior (elasticity and hardness), resembling to commercially available filaments) and were semi-transparent (PVA-based filaments had a yellowish and CA-based filament a brownish color - Figure 2A & B).

3.2. Mechanical tests

3.2.1. Instrumented Indentation Testing (IIT)

Mechanical properties of the filaments appear to be critical for their printability (Aho et al., 2019). The loading-unloading indentation curves of the CA-based and PVA-based filaments are shown in Figure 3A. The indentation force–depth curves for the two materials under test specified a creep phenomenon at the peak force of 150 mN. The CA-based filament has shown somewhat smaller creep at the peak force, while both loading and unloading curves have shown no discontinuities or steps, indicating that no cracks were formed during indentation. The indentation depth at the peak load is 7.3 μm for the PVA-based filament and 8.8 μm for the CA-based filament. Also, the plastic work done was higher for the PVA-based filament, as revealed from the increased area enclosed between the loading and unloading curve. Figure 3B & C shows the results from the indentation test. The modulus of PVA-based formulation was the highest with a value of 2.89 GPa ± 0.26, probably due to the addition of the NaCl and small amount of plasticizer (13% mannitol). It seems that the addition of 25% TEC for the filaments

Journal Pre-proof

created by using the CA-based formulation give a lower value for the elastic modulus, which was measured as 1.72 ± 0.15 GPa. For the indentation hardness measurements, slightly highest values are presented in the PVA-based formulation (137.6 ± 15.59 MPa, followed by the CA-based formulation measuring 123.9 ± 10.67 MPa, although this difference is not statistically significant (t-test, p = 0.14).

In a previous work we showed that printability of the filament is affected by both elastic modulus and hardness (increasing as hardness increases and elastic modulus deceases) (Gioumouxouzis et al., 2018c). More specifically, filaments appeared to be printable when elastic modulus/hardness ratio is approximately lower than 20. In the present work this rule is confirmed as both filaments exhibited acceptable printability when tested, whereas their elastic modulus/hardness ratio is 20.99 for PVA-based formulation and 13.88 for CA-based formulation. These results allow the expansion of the above conclusion stating that filaments with elastic modulus/hardness ratio less than 21 are printable. Moreover, the observation that CA-based filament exhibited superior printability in comparison to the PVA-based filament (resembling to the printability of commercial filaments), allow the conclusion that lowering of elastic modulus/hardness ratio leads to improved filament printability.

3.2.2. Tensile tests

To further assess the mechanical behaviour of the materials under study, a typical tensile test was performed on the produced filaments. It is shown in Figure 4, that the strength of PVA-based formulation is the highest reaching around 55 ± 6.75 MPa, while for the CA-based formulation the strength is lower to around 44 ± 7.75 MPa (t-test, p = 0.13). Evidently, the strain to failure is higher for the CA-based formulation. The modulus calculated from the elastic part of the stress-

Journal Pre-proof

strain response for the CA-based formulation is 1.57 GPa which differs only 8.7% from the value obtained from the indentation tests. Additionally, the modulus for the PVA-based formulation was calculated as 2.43 GPa which differs 15.9% from the values obtained from the indentation tests. The differences are attributed to the possible manufacturing defects of the filaments and the fact that the indentation test measures the local performance of the bulk material, while tensile tests involve a greater amount of material under stress.

3.3. Printing procedure

Adequately uniform covering of the core without defects was achieved only with "purging walls" option activated. Moreover, custom added purging columns were also necessary in order to create dosage forms without over-deposition spots of PVA-based core material that could compromise structural integrity of the shell during dissolution (as it is water-soluble). An image of the dosage form B on the building plate is shown in Figure 2C (purging columns and walls are clearly presented). Figure 2D depicts formulations A & B after removal of the purging structures. It should be noted that material used for these structures can be grinded, extruded and reused for printing purposes. Dimensions and weight of the printed formulations are presented in Table 1.

3.4 Visualization studies

3.4.1. SEM analysis

The external morphological properties of the dosage forms were assessed by means of SEM. In the case of formulations B and C (fully covered) lateral images of the dosage forms revealed an even and homogenous succession of CA of outer shell layers. Fusion between layers was complete (no pores detected), although layers' height uniformity varied significantly (Figure

Journal Pre-proof

5A). Imported linear cavities appear to have a height very close to the designed dimensions (0.2mm – Figure 5B). Top corner images show full covering of the core, despite the fact that layers' overlap was not completely uniform (Figure 5C). Figure 5D shows that imported top and bottom shell holes had a shape slightly deviating from perfect circular, whereas their diameter varied between 750-900 μm. That deviation from the original design (d=1.3 mm) was attributed to the tendency of the molten printed material to spread out slightly after deposition from the moving printhead (Gioumouxouzis et al., 2018b) . More magnified images show that surface of the printed strands was smooth and homogenous (Figure 5E).

Formulation A (no-top cover) top images show perfect fusion between the two layers of the CA shell (Figure 5F), a homogenous and well-arranged succession of layers of the PVA-based core at both center and corner segments (Figure 5G & H) and a sufficient fusion between CA shell and PVA core at their interface (Figure 5I). A magnified image of the PVA-based strands reveals a smooth surface spotted with small NaCl granules (white spots - Figure 5J).

Such NaCl crystalline granules are also present at images of PVA-based filament (Figures 5M & N). Otherwise, both PVA-based and CA-based filaments appear to be compact (no pores present) and present a smooth external surface (Figures 5K & L).

Journal Pre-proof

3.4.2. Elemental analysis

In elemental analysis, diagrams of a random area of the PVA-based core of the formulation indicate that the predominant elements are C (56.04%), O (35.85%) and N (4.64%). Na, Cl (from the incorporated NaCl) and S (present in DIL molecule) are detected in very low percentages (< 2%) (Figure 6A). The percentage of Na and Cl in a random spot of the surface of the osmotic core (Figure 6B) appears to decrease in comparison to their percentage in the area diagram (as they are predominantly concentrated at the white spots – NaCl crystals). White spots appear to be NaCl particles, as focused elemental analysis on them revealed the significant presence of Na and Cl (22.98% and 25.58% respectively – Figure 6C).

3.4.3. Optical microscopy

In optical microscopy images of formulations' B and C imported top holes are presented in Figures 7A & C. Succession of strands is clearly visible in lateral images (Figure 7B & D), as also the imported linear cavities (Figure 7B). Bottom view of these formulation is presented in Figure 7J. whereas Figure 7L shows formulations' B and C top and lateral back view (opposite side of the imported cavities). A close-up view of the imported cavity is also presented at Figure 7K.

Formulations' A top and lateral images are presented in Figure 7E & F. Figure 7I present formulations' A bottom view (no hole imported).

Filament images reveal the consistent diameter (1.7-1.8 mm) of both PVA-based and CA-based filaments. Both filament types present smooth external surfaces, with PVA-based filament exhibiting slightly increased surface roughness (Figure 7G & H).

3.5. Thermogravimetric analysis (TGA)

TGA analysis was employed to determine the water content and polymer stability upon heating (Figure 8). The S.D. of weight loss were not higher than ± 0.3 %.

Regarding to the core composition, TGA thermograms of the raw materials, PVA-based filament and 3D printed core structure showed no mass loss till printing (205^{o}C) or HME (165^{o}C) temperatures. Water loss embedded in filament and raw polymers is depicted as a ~5% mass loss

Journal Pre-proof

till 150^{o}C. Thermostability of DIL, mannitol, PVP K30 is demonstrated, as onset of degradation (220^{o}C (Sorrenti et al., 2010), 303^{o}C (Ong et al., 2014) and 400^{o}C (Okwuosa et al., 2016), respectively), exceeds 3DP temperatures.

For the shell composition a mass loss ~3% observed till 100^{o}C in both CA-based filament and 3DP shell is attributed to water loss. Moreover, a mass reduction starting after 130^{o}C observed in 3DP shell is attributed to gradual evaporation of the incorporated TEC (~15% mass loss till printing temperature (215^{o}C) (Okwuosa et al., 2017). Nevertheless, the actual TEC loss is expected to be far less in 3DP structures since residence time inside heated nozzle in temperatures favouring TEC evaporation is short (less than 1 min) followed by rapid cooling, whereas in TGA residence time in temperatures favouring evaporation was 8.5 min (from 130^{o}C till 215^{o}C, considering heating rate 10^{o}C/min). Furthermore, TEC was added to the formulation as a plasticiser (in order to facilitate HME and printing procedure) and its reduction does not alter the final formulation's functionality, confirmed in dissolution studies.

3.6. Differential scanning calorimetry (DSC)

The DSC thermograms of all samples are demonstrated in Figure 9. The S.D. of thermogram temperatures were not higher than ± 1.0 °C.

The most prominent observation is the disappearance of the endotherm melting peaks of DIL (217^{o}C) (Türk et al., 2009) and mannitol (170^{o}C) (Gombás et al., 2003), indicating potential amorphization in filament and 3DP core structures. Moreover, PVA-based filament's melting temperature (T_m) is lowered by ~30^{o}C in comparison to the raw PVA, because of the plasticising effect of the incorporated mannitol.

Journal Pre-proof

Raw CA melting peak and T_g are observed at 233°C and 194°C, respectively. T_g is significantly lowered in HME filament (112°C), due to the addition of the plasticiser (TEC) and is slightly elevated in 3DP formulations shell (118°C), as a fraction of TEC has evaporated during printing heating. The above results are in accordance to the literature (Zepnik et al., 2013).

3.7. X-ray Powder diffraction (XRD)

The X-ray diffractograms reveal the amorphization of the partially crystalline raw CA (Sun et al., 2013) after HME and 3DP printing (Figure 10B). Pure DIL, NaCl and mannitol exhibit multiple distinct peaks, indicating their crystalline nature. Mannitol representative peaks correspond to beta-D-mannitol (14.85, 18.83, 23.64) (Cares-Pacheco et al., 2014), whereas DIL and NaCl present their characteristic main peaks (10.56, 18.20, 19.51, 22.3) (Türk et al., 2009) and (31.7, 45.4) (Bao et al., 2017), respectively. Mannitol peaks disappear after HME (amorphization), but a characteristic peak appears at 9.6 degrees in 3D printed core structure, signaling recrystallisation of mannitol towards delta polymorph after 3D printing (Cares-Pacheco et al., 2014). DIL also loses its crystallinity after HME and 3DP procedures, whereas NaCl remains crystalline (Figure 10.A), an observation in agreement with SEM images clearly depicting NaCl microparticles inside filament and 3DP core structures. NaCl retains its crystallinity as HME and 3DP procedure temperatures are far below T_m of NaCl (801.4°C) (Broström et al., 2013). This observation is confirmed by TGA diagrams – no mass loss observed till 500°C.

Journal Pre-proof

3.8. *In vitro* release of Diltiazem from 3D printed dosage forms

In Figure 11 are presented the dissolution profiles of different formulations. Formulation A dosage forms start releasing DIL immediately and their dissolution profile follows quadratic kinetics ($F=100*(k_1*t\text{^}2+k_2*t)$, $k_1 = 3.05*10^{-6}$, $k_2 = 1.2*10^{-3}$, $R^2_{adj} = 0.994$). That behavior is attributed to the one-direction dissolution of the core (as only the upper surface of the core was exposed to the dissolution medium during the dissolution process) and the gradually developed osmotic pressure that induced a slight dissolution acceleration, due to gradual full hydration of the osmotic core. This observation is supported by the fact that dissolution procedure of hydrophilic API's from PVA matrices is both erosion/diffusion mediated and follows a relatively steady pattern till the middle of the dissolution process, slightly decelerating thereafter (Harland et al., 1988). In our formulations this steady release pattern was not hindered, but slightly accelerated, due to the osmotic forces induced by gradual water uptake of the core matrix.

On the contrary, formulations B and C present delayed release of the API, attributed to the time required for the shells to open at the imported linear cavities. Figure 2E shows characteristic images indicating the way the formulations B and C have opened (at the exact point of the imported linear cavities) after their exposure at the dissolution medium.

More specifically, Form. B starts releasing DIL after ~360 min (8.21% of DIL released) and Form. C after ~120 min (8.76% of DIL released). Release of DIL in Form. B after 360 min follows the quadratic model ($F=k_1*(t-T_{lag})^{\wedge}0.5+k_2*(t-T_{lag})$, $k_1 = 2.44*10^{-6}$, $k_2 = -2.7*10^{-4}$, $T_{lag} = 96$, $R^2_{adj} = 0.987$), whereas Form. C exhibits zero order release ($F=k_0*(t-T_{lag})$, $k_0 = 0.235$, $T_{lag}= 88.81$, $R^2_{adj} = 0.973$) of DIL after 120 min. These results are justified by the fact that Form. A and B are morphologically similar after opening of the latter and therefore, they release DIL according to the same kinetic model (dissolution accelerated due to the increasing osmotic pressure), resulting at similar dissolution curves (Table II). In Form. C, the second opening reliefs the excessive osmotic pressure, but the remaining is sufficient to prevent the gradual deceleration of the release rate of DIL from the PVA matrix (Harland et al., 1988), resulting in a steady DIL release till the end of the dissolution process (zero order release) and a dissolution

Journal Pre-proof

curve dissimilar to the curves of Form. A and B (Table II). Dissolution process started reaching a plateau for Form. A after 6 h (84.64% at 360 min), for Form. B after 12 h (76.37% at 720 min) and for Form. C after 8 h (87.81% at 480 min). At the completion of the dissolution process (1440 min) Form. A had released 91.17%, Form. B 96.22% and Form. C 92.14% of the theoretically incorporated DIL. Variations from theoretical 100%, are attributed to the variations in diameter of the custom-made filament, that resulted in incorporation of slightly less material into the formulations' cores. Variations in opening times of Form. B and C are also attributed to this fact, as the amount of core material affected the induced osmotic pressure. It can be assumed that industrially made filament with minimum diameter deviations could eliminate these variations.

3.9. Time lapsed X-ray microfocus computed tomography (μCT)

A quantitative evaluation of 'Form A' formulation's behaviour during hydration was conducted by means of time-lapsed μCT. The cross-section of the dry dosage form (Figure 12) before the submersion into the dissolution medium, reveals a relatively solid internal structure, although a number of macro-pores is present, as previously reported for structures 3D printed using PVA-based filaments (Gioumouxouzis et al., 2018b). Bright spots (areas with higher electronic density) correspond to NaCl crystals, as confirmed by elemental analysis. Gradual wetting of the osmotic core (shown at t > 100 min), predominantly through imported linear cavities, results in rise of the internal osmotic pressure and shell rupture, depicted as slow lifting of the upper and lower parts of the shell (Figure 12). It can be observed that as wetting process evolves, hydration of the core results in transformation of the core material into a gel-like homogenous mass and partial dissolution. At t =150 min the volume of the hydrated portion of the remaining core for

Journal Pre-proof

the first time exceeds the volume of the non-hydrated one (Figure 13). This coincides with the measured increase in release rate shown in Figure 12 at t ≈ 150 min for Form A. As time passes, hydration proceeds, and the core swells and dissolves. At t =400 min the wetting of the core appears to have mostly completed. Only a small (7.5 mm^3) core remains “dry” in the center of the core and a sizable fraction of the core material has dissolved into the dissolution medium. The time of completion of the wetting process coincides with the time when cumulative release reaches plateau (Fig. 12) at t =400 min for Form A.

Interestingly, despite the fact that a significant portion of the core has at this stage been dissolved, the total core volume (i.e. the volume of the hydrated and the dry core) appears to remain constant (Figure13). This can be attributed to the increased volume of the hydrated core due to swelling, which compensates for the material loss due to dissolution.

A small but notable amount of swelling also occurs in the CA-shell, the total volume of which increases from 215.5 mm^3 to 258.3 mm^3. Prolonged exposure (t > 200 min) of the shell to the medium and swelling causes dissolution and partial disintegration. This is captured as volume decrease due to material loss for t > 200 min (Figure 13).

It must also be noted that the dissolution process from PVA matrices is achieved through both diffusion and disintegration (Harland et al., 1988), therefore it can be expected that at this stage most of DIL has migrated to the dissolution medium, despite the fact that some core-material is still present in the dosage form.

4. CONCLUSIONS

In the present study was attempted the construction of 3D printed dosage forms consisting of an osmotic core (containing the API diltiazem), covered with a semi-permeable cellulose acetate

Journal Pre-proof

(CA) layer. Three different formulations were created, differing at the shape of the CA shell. Specifically, one and two linear cavities were introduced to the first and the second formulations' shells, respectively, whereas in the third formulation the upper part of the shell was completely removed. Moreover, holes were introduced at the upper and lower shell wall in order to facilitate water permeation. Water uptake resulted in core swelling and shell rupture at the introduced cavities, due to elevated internal osmotic pressure. This behavior led to the *in vitro* delayed release of diltiazem from the dosage form (initiation of release after six hours for the first and after two hours for the second formulation). Additionally, all three formulations appear to attribute the API to the dissolution medium at a steady rate. The above results are confirmed by utilizing μCT, that visualized the gradual wetting of the osmotic core and the subsequent rupture of the dosage forms. These results highlighted the potential transition of pharmaceutical manufacturing towards four-dimensional printing, namely the 3DP of complex formulations, able to modify their shape (and thus their functionality) as a function of time, under the influence of external stimuli.

Journal Pre-proof

ACKNOWLEDGEMENTS

The authors would like to acknowledge μ-VIS X-ray Imaging Centre and the Biomedical Imaging Unit at the University of Southampton for the provision of tomographic imaging facilities, as well as Nikon Metrology UK Ltd for the provision of the Med-X prototype scanner. We also acknowledge the use of the IRIDIS High Performance Computing Facility, and associated support services at the University of Southampton, in the completion of this work and Mr. Antonios Tsiarsiotis (GCODE Workspace) for his help regarding the design of the dosage forms.

CONFLICT OF INTEREST

The authors report no declarations of interest.

REFERENCES

Abd-Elbary, A., Tadros, M.I., Alaa-Eldin, A.A., 2011. Development and in vitro/in vivo evaluation of etodolac controlled porosity osmotic pump tablets. AAPS PharmSciTech 12, 485-495.

Aho, J., Bøtker, J.P., Genina, N., Edinger, M., Arnfast, L., Rantanen, J., 2019. Roadmap to 3D-printed oral pharmaceutical dosage forms: feedstock filament properties and characterization for fused deposition modeling. J. Pharm. Sci. 108, 26-35.

Bao, N., Miao, X., Hu, X., Zhang, Q., Jie, X., Zheng, X., 2017. Novel synthesis of plasmonic Ag/AgCl@TiO2 continues fibers with enhanced broadband photocatalytic performance. Catalysts 7, 117.

BNF, 2014. , in: BMJ Group and the Royal Pharmaceutical Society of Great Britain 2014. pp. 458-460.

Broström, M., Enestam, S., Backman, R., Mäkelä, K., 2013. Condensation in the KCl-NaCl system. Fuel Process. Technol. 105, 142-148.

Cares-Pacheco, M.G., Vaca-Medina, G., Calvet, R., Espitalier, F., Letourneau, J.J., Rouilly, A., Rodier, E., 2014. Physicochemical characterization of d-mannitol polymorphs: The challenging surface energy determination by inverse gas chromatography in the infinite dilution region. Int. J. Pharm. 475, 69-81.

Chai, X., Chai, H., Wang, X., Yang, J., Li, J., Zhao, Y., Cai, W., Tao, T., Xiang, X., 2017. Fused

Journal Pre-proof

deposition modeling (FDM) 3D printed tablets for intragastric floating delivery of domperidone. Sci. Rep. 7, 2829.

Gioumouxouzis, C.I., Karavasili, C., Fatouros, D.G., 2018a. Recent advances in pharmaceutical dosage forms and devices using additive manufacturing technologies. Drug Discov. Today 24, 636-643.

Gioumouxouzis, C.I., Baklavaridis, A., Katsamenis, O.L., Markopoulou, C.K., Bouropoulos, N., Tzetzis, D., Fatouros, D.G., 2018b. A 3D printed bilayer oral solid dosage form combining metformin for prolonged and glimepiride for immediate drug delivery. Eur. J. Pharm. Sci. 120, 40-52.

Gioumouxouzis, C.I., Chatzitaki, A.-T., Karavasili, C., Katsamenis, O.L., Tzetzis, D., Mystiridou, E., Bouropoulos, N., Fatouros, D.G., 2018c. Controlled release of 5-Fluorouracil from alginate beads encapsulated in 3D printed pH-responsive solid dosage forms. AAPS PharmSciTech 19, 3362-3375.

Gioumouxouzis, C.I., Katsamenis, O.L., Bouropoulos, N., Fatouros, D.G., 2017. 3D printed oral solid dosage forms containing hydrochlorothiazide for controlled drug delivery. J. Drug Deliv. Sci. Technol. 40, 164-171.

Gombás, Á., Szabó-Révész, P., Regdon, G., Eros, I., 2003. Study of thermal behaviour of sugar alcohols. J. Therm. Anal. Calorim. 73, 615-621.

Goyanes, A., Wang, J., Buanz, A., Martinez-Pacheco, R., Telford, R., Gaisford, S., Basit, A.W., 2015. 3D Printing of medicines: engineering novel oral devices with unique design and drug release characteristics. Mol. Pharm. 12, 4077-4084.

Harland, R.S., Gazzaniga, A., Sangalli, M.E., Colombo, P., Peppas, N.A., 1988. Drug/polymer matrix swelling and dissolution. Pharm. Res. 5, 488-494.

Journal Pre-proof

Kadry, H., Al-Hilal, T.A., Keshavarz, A., Alam, F., Xu, C., Joy, A., Ahsan, F., 2018. Multi-purposable filaments of HPMC for 3D printing of medications with tailored drug release and timed-absorption. Int. J. Pharm. 544, 285-296.

Khaled, S.A., Burley, J.C., Alexander, M.R., Yang, J., Roberts, C.J., 2015a. 3D printing of five-in-one dose combination polypill with defined immediate and sustained release profiles. J. Control. Release 217, 308-314.

Khaled, S.A., Burley, J.C., Alexander, M.R., Yang, J., Roberts, C.J., 2015b. 3D printing of tablets containing multiple drugs with defined release profiles. Int. J. Pharm. 494, 643-650.

Li, Q., Wen, H., Jia, D., Guan, X., Pan, H., Yang, Y., Yu, S., Zhu, Z., Xiang, R., Pan, W., 2017. Preparation and investigation of controlled-release glipizide novel oral device with three-dimensional printing. Int. J. Pharm. 525, 5-11.

Lim, S.H., Kathuria, H., Tan, J.J.Y., Kang, L., 2018. 3D printed drug delivery and testing systems - a passing fad or the future? Adv. Drug Deliv. Rev. 132, 139-168.

Mansour, G., Tzetzis, D., 2013. Nanomechanical characterization of hybrid multiwall carbon nanotube and fumed silica epoxy nanocomposites. Polym. - Plast. Technol. Eng. 52, 1054-1062.

Mansour, G., Tzetzis, D., Bouzakis, K.D., 2013. A nanomechanical approach on the measurement of the elastic properties of epoxy reinforced carbon nanotube nanocomposites. Tribol. Ind. 35, 190-199.

McClelland, G.A., Sutton, S.C., Engle, K., Zentner, G.M., 1991. The solubility-modulated osmotic pump: In vitro/in vivo release of diltiazem hydrochloride. Pharm. Res. 8, 88-92.

Mohanty, A.K., Wibowo, A., Misra, M., Drzal, L.T., 2003. Development of renewable resource-based cellulose acetate bioplastic: effect of process engineering on the performance of cellulosic plastics. Polym. Eng. Sci. 43, 1151-1161.

Journal Pre-proof

O'Neil, M.J. (Ed.), 2013. The Merck Index - An Encyclopedia of Chemicals, Drugs, and Biologicals. Royal Society of Chemistry, Cambridge, UK.

Okwuosa, T.C., Pereira, B.C., Arafat, B., Cieszynska, M., Isreb, A., Alhnan, M.A., 2017. Fabricating a shell-core delayed release tablet using dual FDM 3D printing for patient-centred therapy. Pharm. Res. 34, 427-437.

Okwuosa, T.C., Stefaniak, D., Arafat, B., Isreb, A., Wan, K.W., Alhnan, M.A., 2016. A lower temperature FDM 3D printing for the manufacture of patient-specific immediate release tablets. Pharm. Res. 33, 2704-2712.

Ong, H.X., Traini, D., Ballerin, G., Morgan, L., Buddle, L., Scalia, S., Young, P.M., 2014. Combined inhaled salbutamol and mannitol therapy for mucus hyper-secretion in pulmonary diseases. AAPS J. 16, 269-280.

Park, H.M., Misra, M., Drzal, L.T., Mohanty, A.K., 2004. "Green" nanocomposites from cellulose acetate bioplastic and clay: Effect of eco-friendly triethyl citrate plasticizer. Biomacromolecules 5, 2281-2288.

Pereira, B.C., Isreb, A., Forbes, R.T., Dores, F., Habashy, R., Petit, J.-B., Alhnan, M.A., Oga, E.F., 2019. 'Temporary Plasticiser': A novel solution to fabricate 3D printed patient-centred cardiovascular 'Polypill' architectures. Eur. J. Pharm. Biopharm. 135, 94-103.

Pietrzak, K., Isreb, A., Alhnan, M.A., 2015. A flexible-dose dispenser for immediate and extended release 3D printed tablets. Eur. J. Pharm. Biopharm. 96, 380-387.

Scoutaris, N., Ross, S.A., Douroumis, D., 2018. 3D printed "starmix" drug loaded dosage forms for paediatric applications. Pharm. Res. 35, 34.

Sorrenti, M., Catenacci, L., Bonferoni, M.C., Sandri, G., Caramella, C., Bettinetti, G.P., 2010. Thermal characterization of diltiazem and λ-carrageenan binary systems. J. Therm. Anal.

Journal Pre-proof

Calorim. 102, 337-342.

Stepanovs, D., Jure, M., Gosteva, M., Popelis, J., Kiselovs, G., Mishnev, A., 2016. Crystal structures and physicochemical properties of diltiazem base and its acetylsalicylate, nicotinate and L-malate salts. CrystEngComm 18, 1235-1241.

Sun, X., Lu, C., Zhang, W., Tian, D., Zhang, X., 2013. Acetone-soluble cellulose acetate extracted from waste blended fabrics via ionic liquid catalyzed acetylation. Carbohydr. Polym. 98, 405-411.

Tagami, T., Nagata, N., Hayashi, N., Ogawa, E., Fukushige, K., Sakai, N., Ozeki, T., 2018. Defined drug release from 3D-printed composite tablets consisting of drug-loaded polyvinylalcohol and a water-soluble or water-insoluble polymer filler. Int. J. Pharm. 543, 361-367.

Türk, C.T., Hasçiçek, C., Gönül, N., 2009. Evaluation of drug-polymer interaction in polymeric microspheres containing diltiazem hydrochloride. J. Therm. Anal. Calorim. 95, 865-869.

Tzetzis, D., Mansour, G., Tsiafis, I., Pavlidou, E., 2013. Nanoindentation measurements of fumed silica epoxy reinforced nanocomposites. J. Reinf. Plast. Compos. 32, 160-173.

Verma, R., 2002. Formulation aspects in the development of osmotically controlled oral drug delivery systems. J. Control. Release 79, 7-27.

Yalkowsky, S.H., He, Y., Jain, P., 2010. Handbook of Aqueous Solubility Data, CRC Press.

Yushkevich, P.A., Piven, J., Hazlett, H.C., Smith, R.G., Ho, S., Gee, J.C., Gerig, G., 2006. User-guided 3D active contour segmentation of anatomical structures: Significantly improved efficiency and reliability. Neuroimage 31, 1116-1128.

Zepnik, S., Hildebrand, T., Kabasci, S., Ra-dusch, H.-J., Wodke, T., 2013. Cellulose acetate for thermoplastic foam extrusion, in: Cellulose - Biomass Conversion. InTech. DOI: 10.5772/56215

Journal Pre-proof

Zhang, Y., Huo, M., Zhou, J., Zou, A., Li, W., Yao, C., Xie, S., 2010. DDSolver: An add-in program for modeling and comparison of drug dissolution profiles. AAPS J. 12, 263-271

Journal Pre-proof

Graphical Abstract

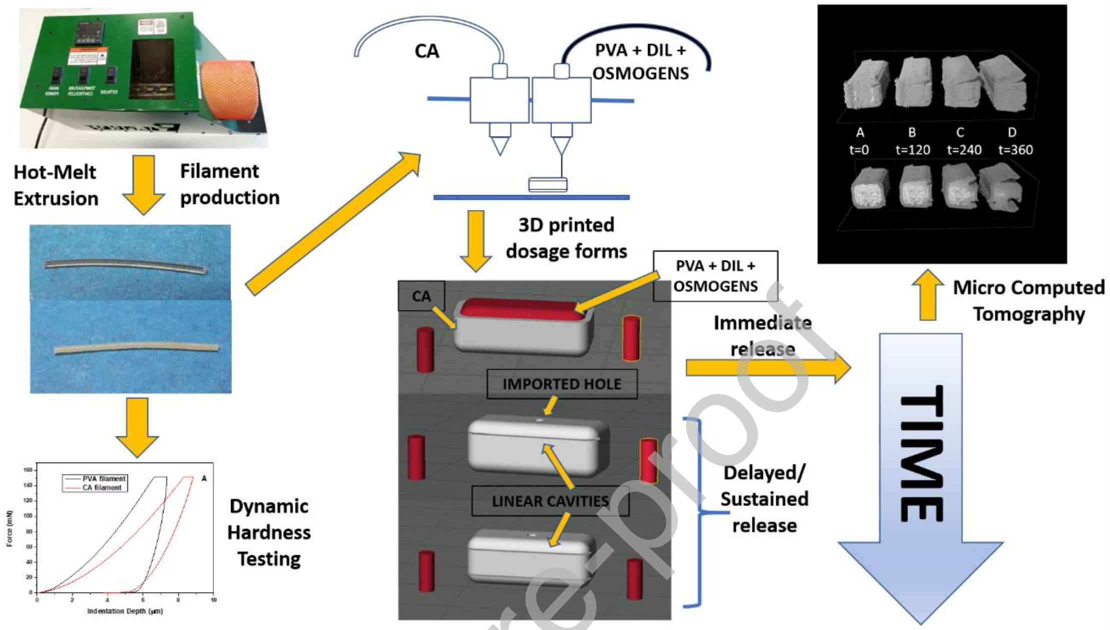

Journal Pre-proof

Table I

Measured properties of 3D printed formulations **(A), (B)** and **(C)** (n=3 ± S.D.). % divergences of measured properties of 3D printed formulations **(A), (B)** and **(C)** from theoretically targeted values.

Formulations	Length (mm)	Divergence %	Width (mm)	Divergence %	Height (mm)	Divergence %	Printed dosage form Weight (mg)
A (no top)	16.12± 0.07	-0.51	6.92 ± 0.07	2.82	5,68 ± 0.5	1.43	639.80 ± 21.82
B (single-cavity)	16.08 ± 0.12	-0.74	6.88 ± 0.10	2.23	6.19 ± 0.3	0.16	674.96 ± 19.48
C (double-cavity)	16.17 ± 0.10	-0.18	6.87 ± 0.08	2.08	6.16 ± 0.6	0.64	668.31 ± 22.39

Table II

Similarity factor (f_2) of the release profiles obtained from 3D printed Formulations. Similarity was indicated as accepted (+) or rejected (-).

Formulation	f_2	Similarity
A-B	53.8	+
A-C	23.5	-
B-C	26.6	-

Journal Pre-proof

FIGURE LEGENDS

Figure 1. Makerware® .stl images of: **A**) formulation A (No-top), **B**) formulation B (Single-cavity) and **C**) formulation C (Dual-cavity).

Figure 2. Images of: **A**) PVA-based filaments, **B**) CA-based filaments, **C**) printed dosage forms and purging structures (walls, columns) on the building plate, D) printed formulations (A and B type) and **D**) empty opened shells at the end of the dissolution process (B and C type).

Figure 3. A) Typical force-depth curves of PVA- and CA-based filaments, **B**) Hardness and **C**) elastic modulus results obtained from the loading-unloading indentation curves of PVA- and CA-based filaments.

Figure 4. Typical tensile stress-strain curves of PVA- and CA-based filaments.

Figure 5. SEM images of formulations B and C: **A**) shell lateral view, **B**) imported linear cavities, **C**) top corner view, **D**) top and bottom shell holes and **E**) printed shell surface close-up. SEM images of formulation A: **F**) top shell wall view, **G**) top view PVA core center image, **H**) top view PVA core corner image, **I**) CA shell and PVA core interface and **J**) PVA core close-up. SEM images of: **K**) CA-based filament cross-section, **L**) CA-based filament close-up, M) PVA-based filament cross-section and **N**) PVA-based filament close-up.

Journal Pre-proof

Figure 6. Elemental analysis (% percentage of constituent elements) of: **A**) osmotic core surface random area, **B**) osmotic core surface random spot and **C**) osmotic core surface random white spot.

Figure 7. Optical microscopy images of formulations B and C: **A**) top shell view, **B, D**) shell lateral views, **C**) shell top hole. Optical microscopy images of formulation A: **E**) top view, **F**) lateral view. Optical microscopy images of: **G**) PVA-based filaments and **H**) CA-based filaments. Optical microscopy images of: **I**) formulation A bottom view, **J**) formulation B bottom view, **K**) formulation B top shell hole, **L**) formulation B lateral view (opposite of cavities).

Figure 8. TGA thermograms of API's, excipients, HME produced filaments and 3D printed formulations of: **A**) PVA-based core material and **B**) CA-based shell material.

Figure 9. DSC thermograms of API's, excipients, HME produced filaments and 3D printed formulations of: **A**) PVA-based core material and **B**) CA-based shell material.

Figure 10. XRD diagrams of API's, excipients, their physical mixtures, HME produced filaments and 3D printed formulations of: **A**) PVA-based core material and **B**) CA-based shell material.

Figure 11. Cumulative (%) DIL release from formulation **A** (no top), **B** (single-cavity) and **C** (double-cavity).

Journal Pre-proof

Figure 12. Time-lapsed X-ray microfocus computed tomography (μCT) imaging of the volumetric changes over time during hydration of Form-A formulation: **A)** Volume rendering of the dosage form at t =0 (dry), 100, 200 and 400 min exposure to the dissolution medium; **B)** Clipped views showing the wetting over time, and its effect on both the core and the structure of the CA-shell. Bright spots correspond to NaCl crystals. Gradual wetting of the osmotic results in rise of the internal osmotic pressure and shell rupture (t =100, 200, 400 min). **C)** Cross-sectional views of the formulation showing the development of the hydration process (dry core in green; wet core in cyan) as well as the swelling of the CA-core (t =100, 200 min) which eventually leads to dissolution and partial disintegration (t = 400 min). **D)** Composite volume rendering of the segmented components showing the development of the hydration process in space. For better clarity the wet core component (cyan) is also rendered with respect to the dry component (green). At t =100 min wet and dry components lay entangled side-by-side, splitting the core into two distinct compartments. With time, dissolution medium completely wets the outer part of the core (t =200 min) and start working its way to the centre (t =400 min). At these staged the dry component is fully embedder into the wet.

Figure 13. Volumetric changes over time during hydration of Form-A formulation, as measured by means of μCT. Red line corresponds to the total volume of the CA-shell, while green and blue correspond to the dry and the hydrated portions of the core respectively. Yellow line corresponds to the total volume of the undissolved core material at any given time (Total core volume = Core-dry + Core-wet).

Journal Pre-proof

FIGURE 1

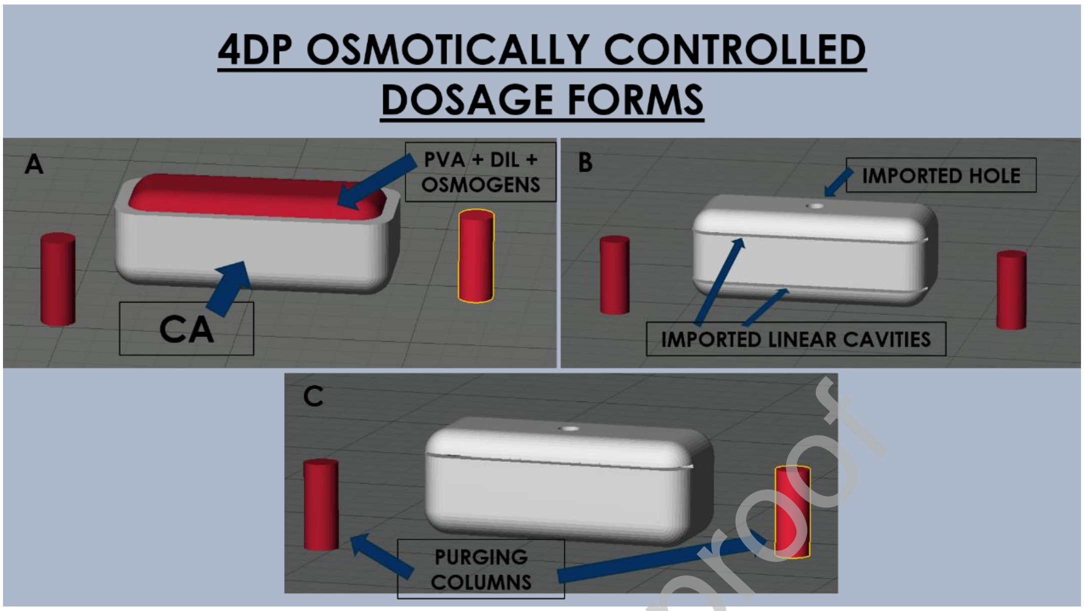

Journal Pre-proof

FIGURE 2

Journal Pre-proof

FIGURE 3

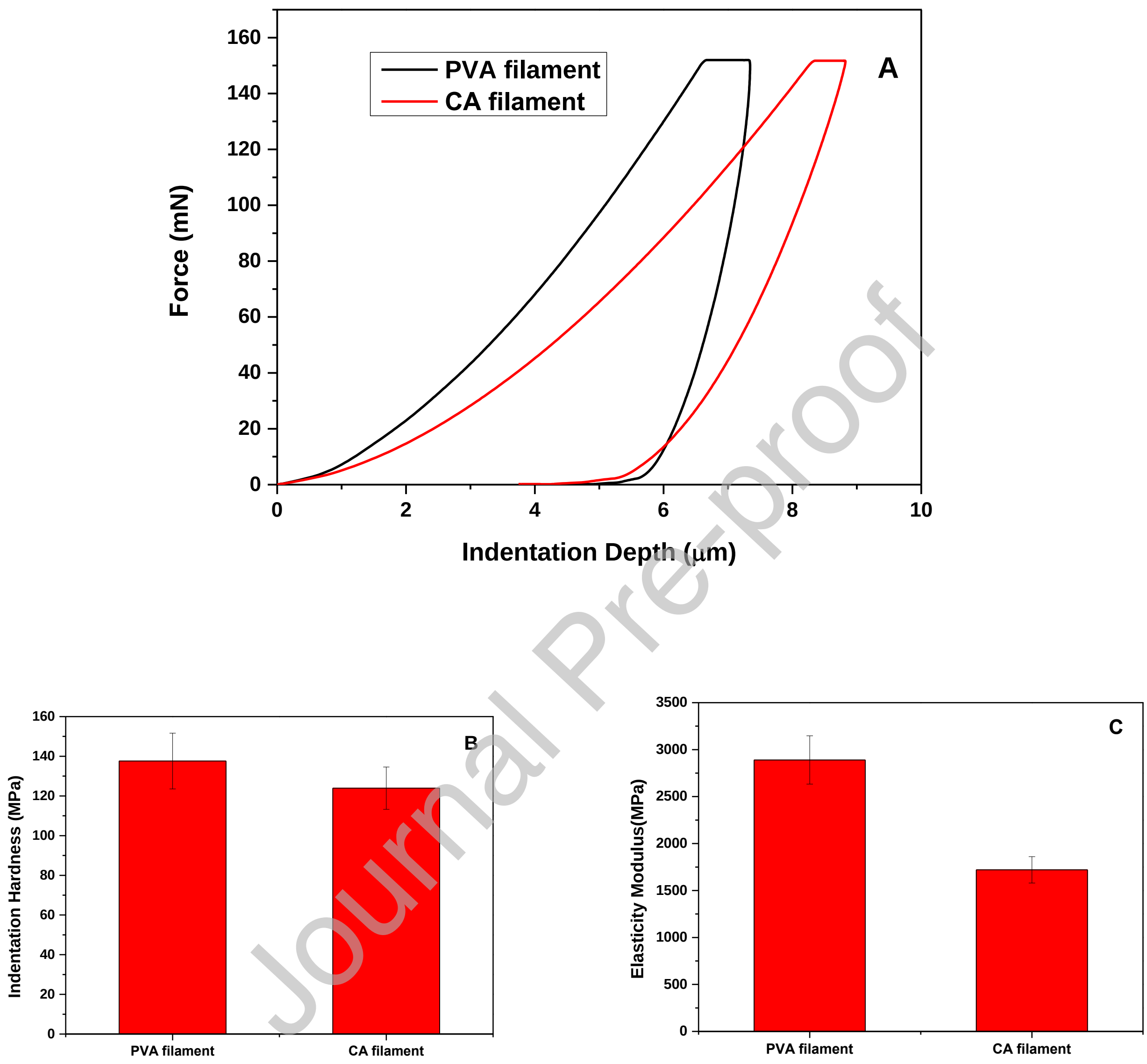

Journal Pre-proof

FIGURE 4

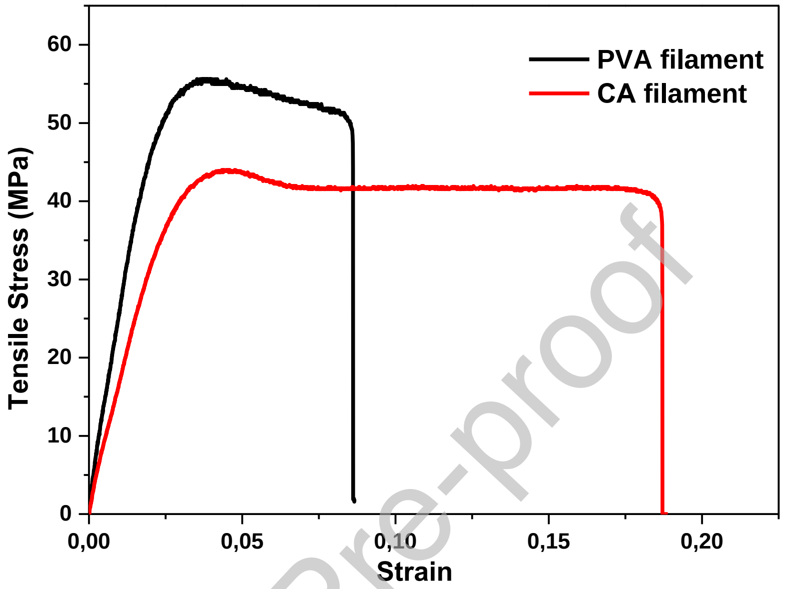

Journal Pre-proof

FIGURE 5

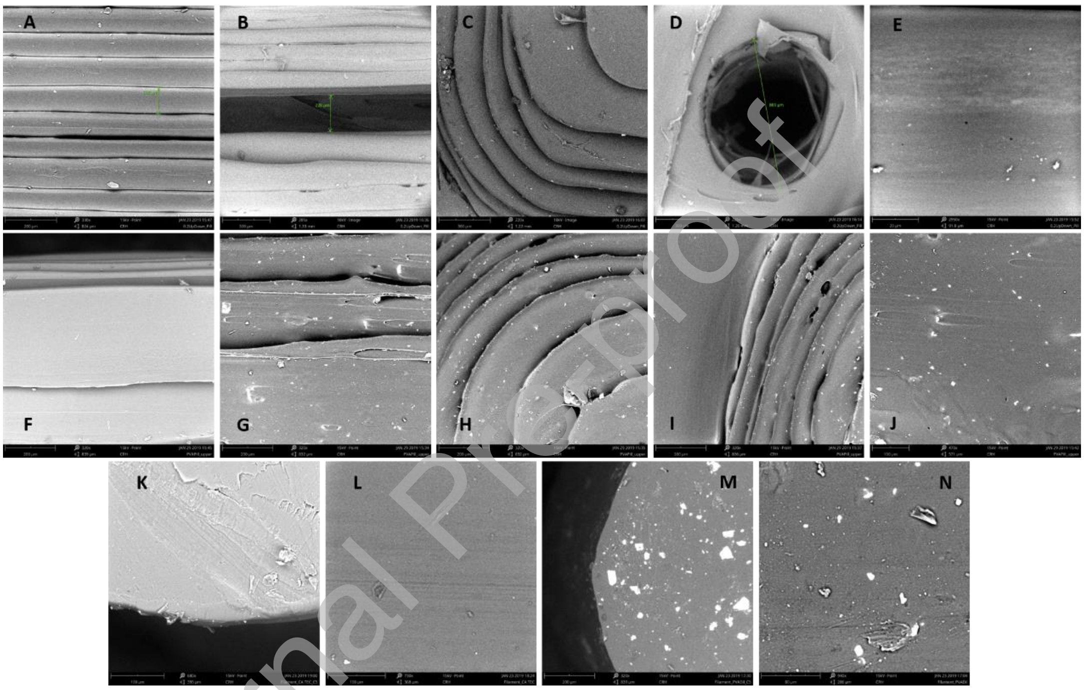

Journal Pre-proof

1. AREA **A**

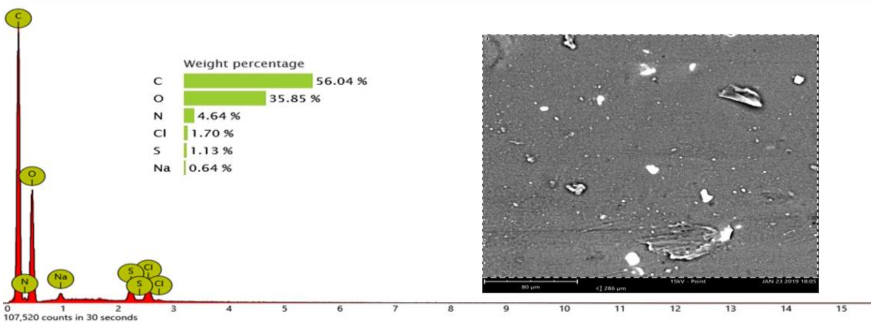

2. SPOT **B**

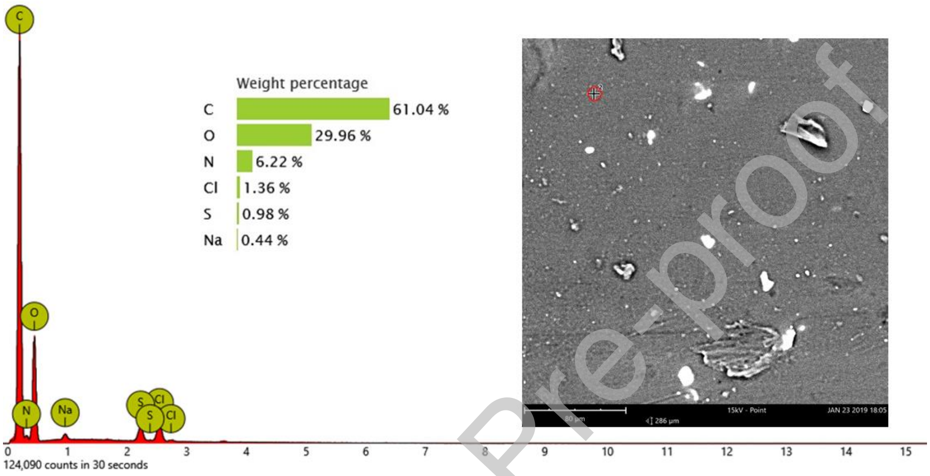

3. SPOT **C**

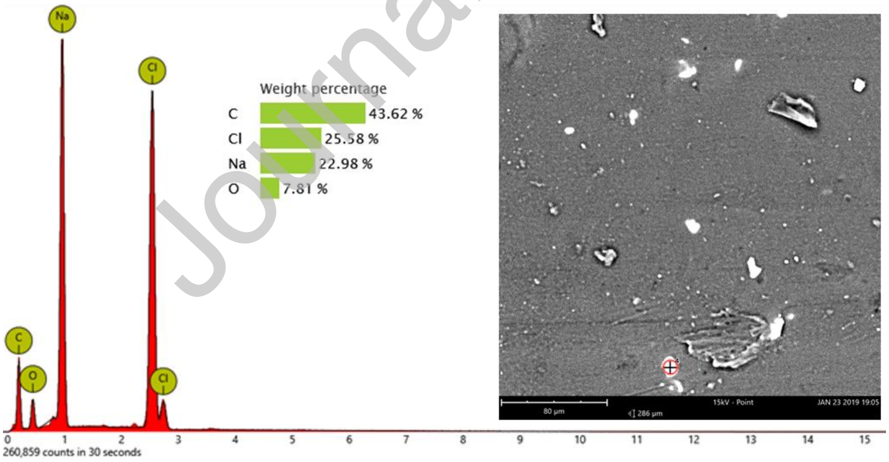

Journal Pre-proof

FIGURE 6

FIGURE 7

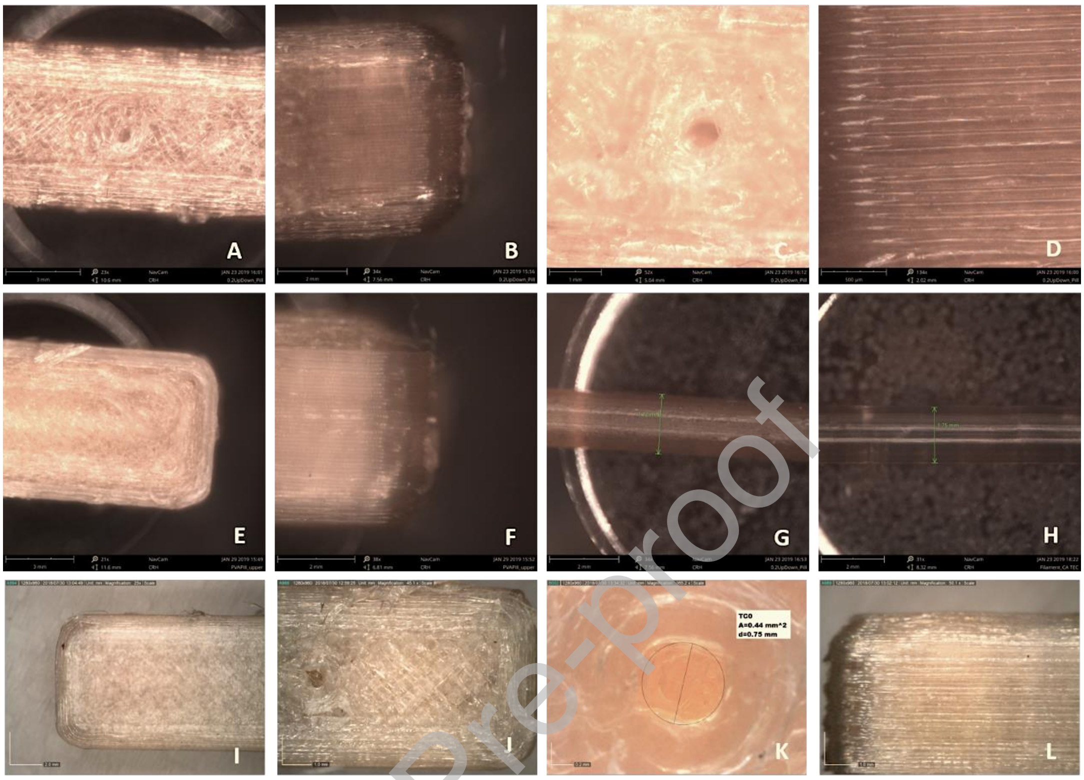

Journal Pre-proof

FIGURE 8

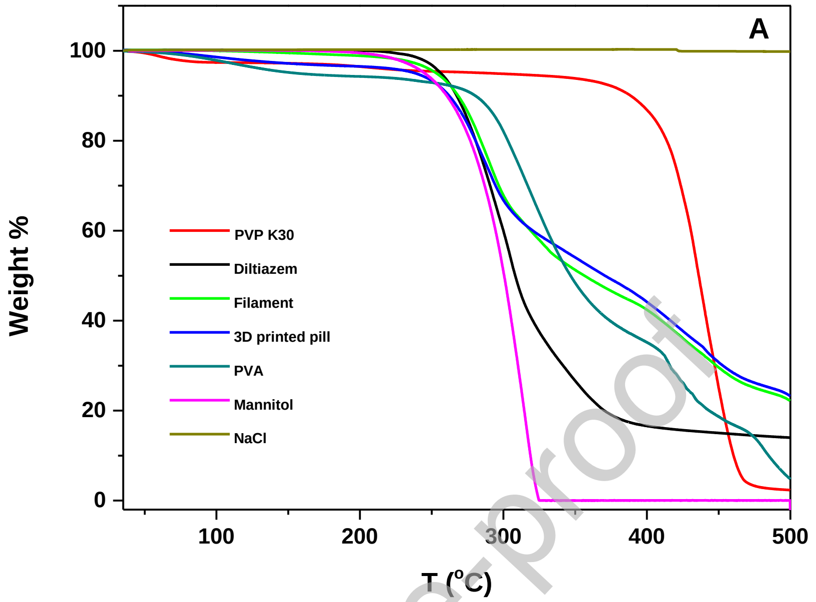

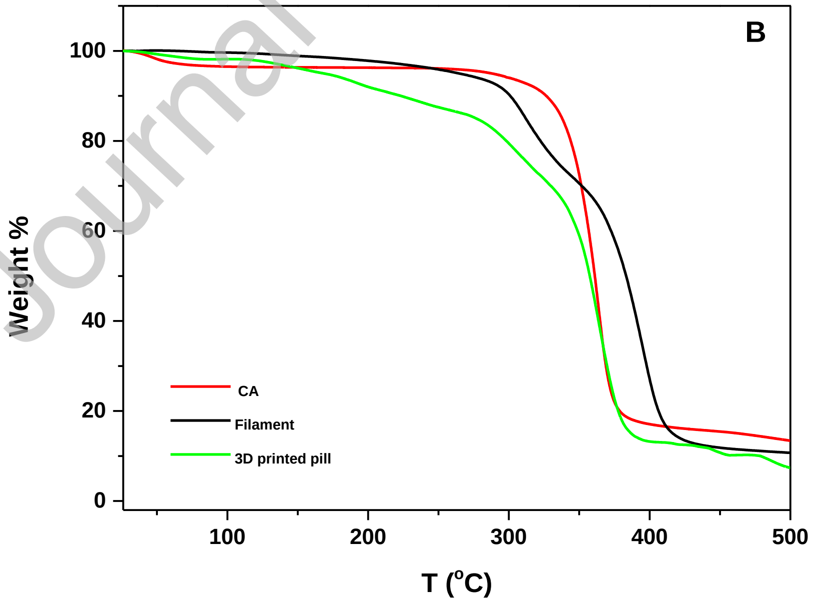

Journal Pre-proof

FIGURE 9

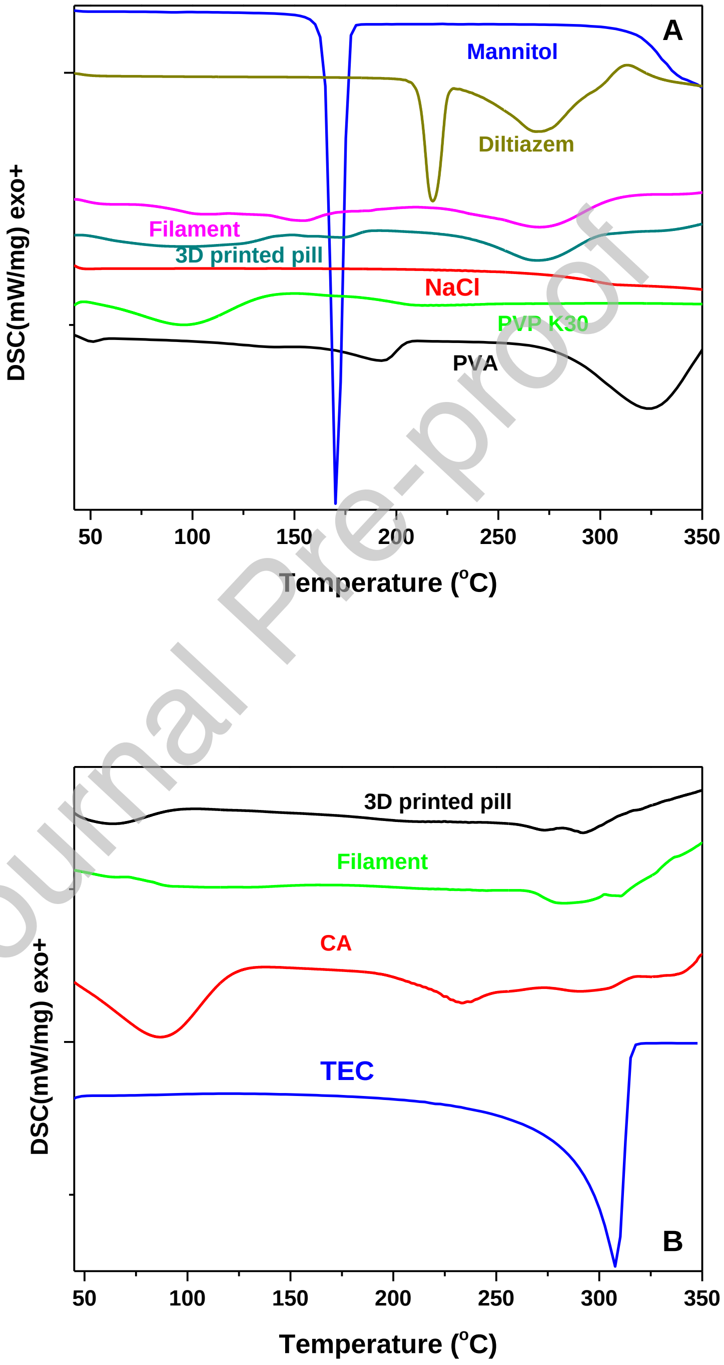

Journal Pre-proof

FIGURE 10

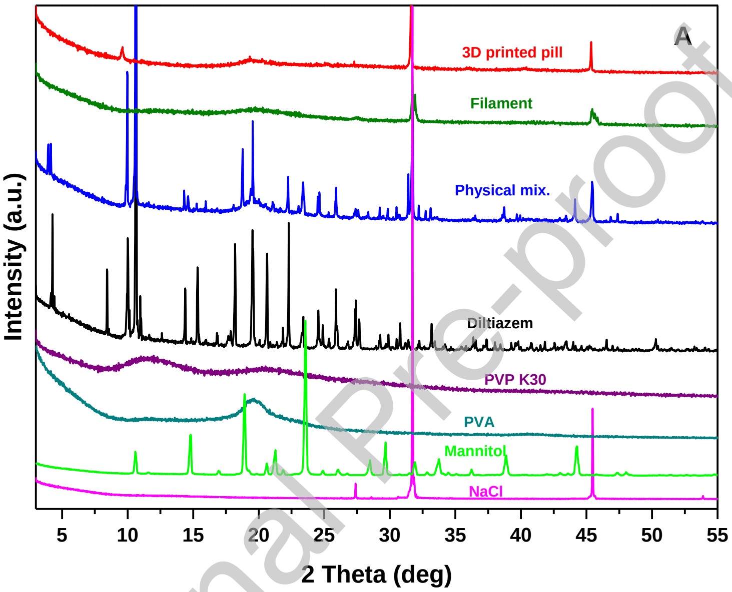

Journal Pre-proof

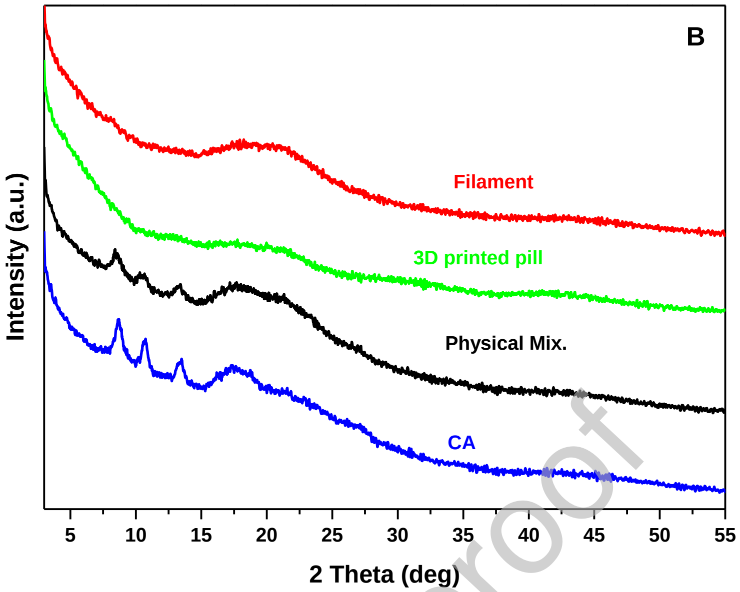

FIGURE 11

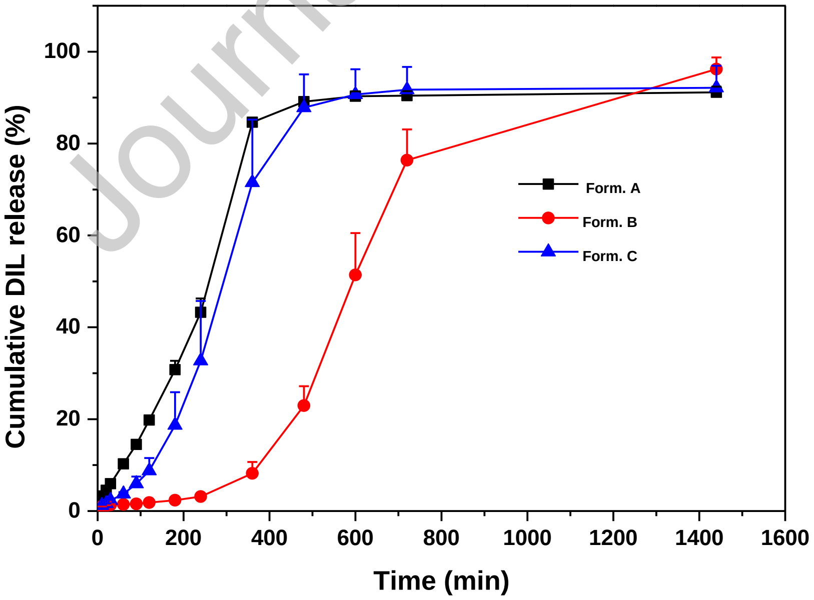

Journal Pre-proof

FIGURE 12

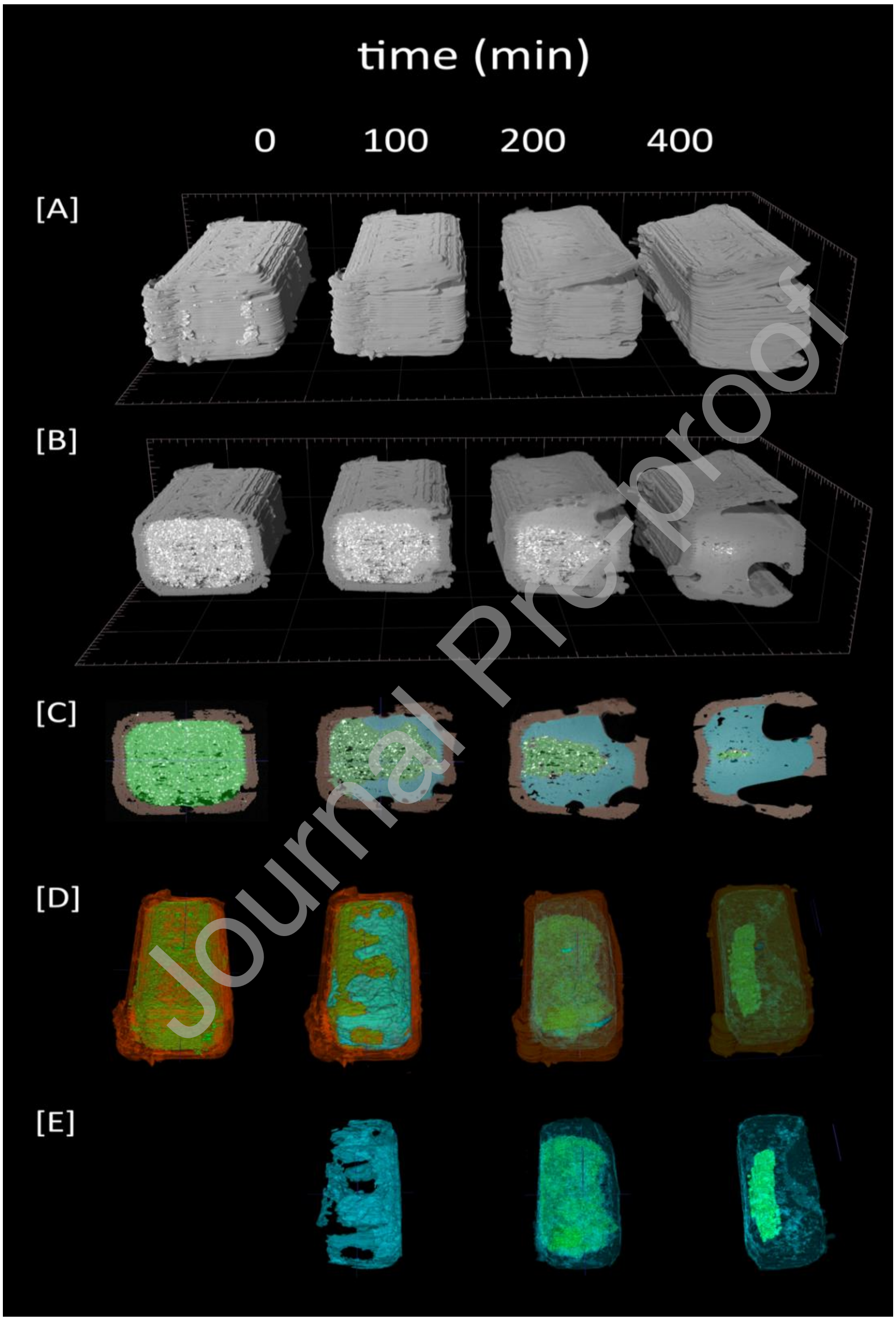

Journal Pre-proof

FIGURE 13

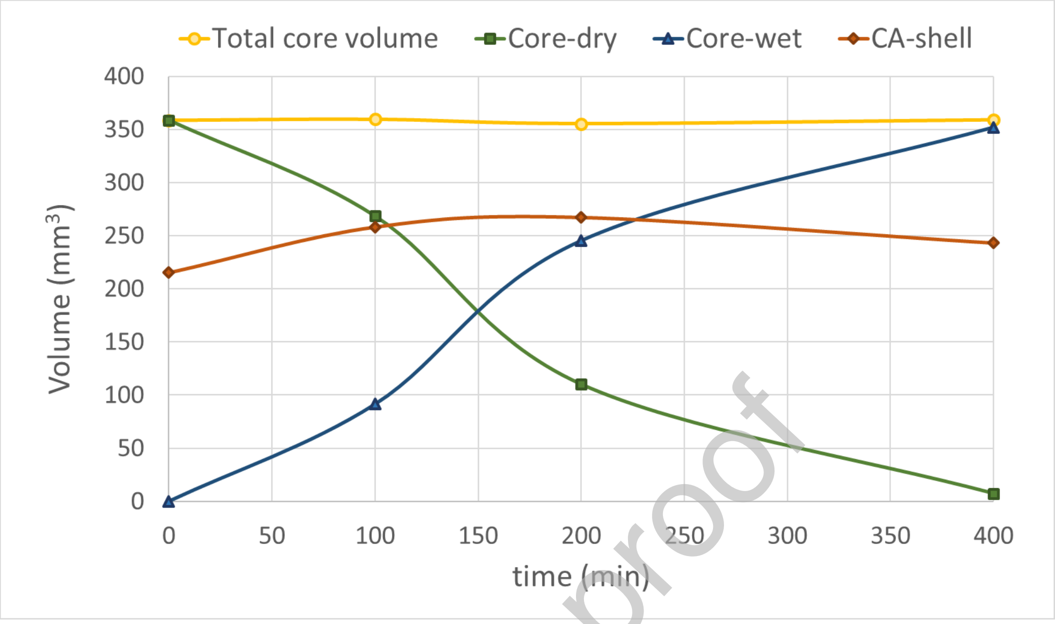

Journal Pre-proof